Eur. Phys. J. A **17**, 37–47 (2003)
DOI 10.1140/epja/i2002-10141-6

THE EUROPEAN PHYSICAL JOURNAL A

Quadrupole collectivity of neutron-rich neon isotopes

R.R. Rodríguez-Guzmán[1], J.L. Egido[2], and L.M. Robledo[2,a]

[1] Institut für Theoretische Physik der Universität Tübingen, Auf der Morgenstelle 14, D-72076 Tübingen, Germany
[2] Departamento de Física Teórica C-XI, Universidad Autónoma de Madrid, 28049-Madrid, Spain

Received: 19 Novemeber 2002 / Revised version: 23 January 2003 /
Published online: 8 April 2003 –
Communicated by G. Orlandini

Abstract. The Angular Momentum Projected Generator Coordinate Method, with the quadrupole moment as collective coordinate and the Gogny force (D1S) as the effective interaction, is used to describe the properties of the ground state and low-lying excited states of the even-even neon isotopes $^{20-34}$Ne, that is, from the stability valley up to the drip line. It is found that the ground state of the $N = 20$ nucleus ^{30}Ne is deformed but to a lesser extent than the $N = 20$ isotope of the magnesium. In the calculations, the isotope ^{32}Ne is at the drip line in good agreement with other theoretical predictions. On the other hand, rather good agreement with experimental data for many observables is obtained.

PACS. 21.60.Jz Hartree-Fock and random-phase approximation – 21.60.-n Nuclear-structure models and methods – 21.10.Re Collective levels – 21.10.Ky Electromagnetic moments

1 Introduction

The properties of the ground and lowest-lying excited states of nuclei close to the stability valley are determined to a great extent by the underlying mean field in which all the nucleons move. The nuclear mean field, obtained through the mean-field approximation to the nuclear many-body problem, provides the important concepts of magic numbers (or shell closures) and that of spontaneous symmetry breaking. For nuclei with proton and/or neutron numbers close to the magic ones symmetry-conserving (*i.e.* non-superconducting and spherical) ground states are expected. On the other hand, nuclei away from the magic configurations are expected to show strong symmetry breaking at the mean-field level leading to deformed (and superconducting) ground states which are the heads of bands generated kinematically by restoring the broken symmetries —like the well-known example of the rotational bands.

Almost thirty years ago, experimental evidences were found in the neutron-rich light nuclei around ^{31}Na [1,2] pointing to the breaking of the $N = 20$ magic number. The first attempt to understand the phenomenon from a theoretical point of view [3] suggested that correlations beyond the mean field coming from the restoration of the rotational symmetry could be strong enough as to overcome the mean-field shell effects and lead to deformed ground states for closed-shell nuclei like ^{31}Na and ^{32}Mg. Further theoretical studies using the Shell Model (SM) approach were carried out [4,5] and it was suggested that an intruder configuration consisting of a two-particle two-hole neutron excitation from the *sd* shell into the $f_{7/2}$ one was the responsible for the deformation in the ground state of ^{32}Mg.

The recent availability of Radioactive Ion Beam facilities in several laboratories like Ganil, GSI, MSU and Riken to cite a few and the development of very efficient mass separators and solid-state detectors has made possible to measure up many properties concerning the ground state and the lowest-lying excited states of many exotic, neutron-rich light nuclei. In particular, the exploration of both the $N = 20$ and $N = 28$ shell closures far from stability has proven to be a rich source of new phenomena. Among the variety of available experimental data, the most convincing evidence for a deformed ground state in the region around $N = 20$ is found in the ^{32}Mg nucleus, where both the excitation energies of the lowest-lying 2^+ [6] and 4^+ [7] states and the $B(E2, 0^+ \to 2^+)$ transition probability [8] have been measured. The low excitation energy of the 2^+ state, the high value of the $B(E2)$ transition probability and also the ratio $E(4_1^+)/E(2_1^+) = 2.6$ are fairly compatible with the expectations for a rotational band. Additional evidence comes from the neighboring isotope ^{34}Mg, where the $E(2_1^+)$ is only 0.66 MeV, the $B(E2, 0^+ \to 2^+)$ is 631 $e^2\text{fm}^2$ and the $E(4_1^+)/E(2_1^+)$ ratio is 3.2, that is, the 0_1^+, 2_1^+ and 4_1^+ satisfy all the requirements to belong to a strongly deformed rotational band [9,10].

[a] e-mail: Luis.Robledo@uam.es

From a theoretical point of view, the ground state of ^{32}Mg is spherical at the mean-field level. However, when the zero-point rotational energy correction (ZPRE) stemming from the restoration of the rotational symmetry is considered, the energy landscape as a function of the quadrupole moment changes dramatically and ^{32}Mg becomes deformed [3,11–14]. A more careful analysis of the energy landscape including the ZPRE correction reveals that, in fact, there are two coexistent configurations (prolate and oblate) with similar energies indicating thereby that configuration mixing of states with different quadrupole intrinsic deformation has to be considered. Therefore, an Angular Momentum Projected Generator Coordinate Method (AMP-GCM) calculation with the quadrupole moment as collective coordinate is called for. We have applied this method in ref. [15] to the study of the nuclei $^{30-34}$Mg with the Gogny force. We have obtained prolate ground states for $^{32-34}$Mg indicating that the $N = 20$ shell closure is not preserved for the Mg isotopes. Moreover, a good agreement with the experimental data for the 2^+ excitation energies and $B(E2)$ transition probabilities was obtained. The method has been used to study quadrupole collectivity of the Si isotopes [16], the $N = 28$ isotopes [17] as well as the superdeformed band in ^{32}S [18] with quite a good success.

The purpose of this paper is to extend the AMP-GCM calculations to the study of the neon (two protons less than magnesium) isotopes from $A = 20$ up to $A = 34$. Contrary to the magnesium isotopic chain, the neon neutron drip line ($N = 22$) is very close to the neutron magic number $N = 20$ and therefore the study of the neon isotopes is a good testing ground to examine both the systematic of deformation and the possible erosion of the $N = 20$ spherical shell closure very close to the neutron drip line. Another interesting point is the study of the possible magicity of $N = 16$ suggested in recent analyses [19].

The paper is organized as follows: In sect. 2 a brief overview of the theoretical framework is presented. In sect. 3.1 the mean-field results are discussed. In the next section the effect of angular momentum projection on the mean-field observables is described. Finally, in sect. 3.3 the results of the configuration mixing calculations are presented and compared to the experimental data and other theoretical approaches. We end up with the conclusions in sect. 4.

2 Theoretical framework

As mentioned in the introduction ours is a mean-field–based procedure where the underlying mean field is determined first and then additional correlations beyond the mean field are included. Those additional correlations are handled in the framework of the Angular Momentum Projected Generator Coordinate Method (AMP-GCM) with the mass quadrupole moment as generating coordinate. As we restrict ourselves to axially symmetric configurations, we use the following ansatz for the $K = 0$ AMP-GCM wave functions,

$$\left|\Phi^I_\sigma\right\rangle = \int \mathrm{d}q_{20} f^I_\sigma(q_{20}) \hat{P}^I_{00} \left|\varphi(q_{20})\right\rangle . \tag{1}$$

For each angular momentum I the different AMP-GCM states (labelled by σ) are linear combinations of the set of angular momentum projected intrinsic wave functions $|\varphi(q_{20})\rangle$ generated by solving the Hartree-Fock-Bogoliubov (HFB) equation constrained to yield the desired mass quadrupole moment $q_{20} = \langle\varphi(q_{20})| z^2 - 1/2(x^2 + y^2) |\varphi(q_{20})\rangle$.

The intrinsic wave functions are restricted to be axially symmetric (*i.e.* $K = 0$) and are obtained by solving the HFB equation with the Gogny interaction [20] (D1S parameterization [21]). The HFB equation is discretized by expanding the quasiparticle operators associated to the intrinsic wave functions $|\varphi(q_{20})\rangle$ in a Harmonic-Oscillator (HO) basis containing eleven major shells and with equal oscillator lengths (in order to make the basis closed under rotations [22]). As we are dealing with quite light systems we have to consider the center-of-mass problem. This is handled by subtracting the center-of-mass kinetic energy both in the calculation of the energy and in the HFB variational procedure. Finally, concerning the Coulomb interaction, we have only taken into account its contribution to the direct field in the variational procedure. The exchange Coulomb energy (computed in the Slater approximation) is added, in a perturbative fashion, at the end of the calculation and the contribution of the Coulomb interaction to the pairing energy is completely disregarded.

In order to obtain the angular momentum projected wave functions we use the standard angular momentum projector operator restricted to $K = 0$ states [23],

$$\hat{P}^I_{00} = \frac{(2I+1)}{8\pi^2} \int \mathrm{d}\Omega \mathrm{d}^I_{00}(\beta) e^{-i\alpha\hat{J}_z} e^{-i\beta\hat{J}_y} e^{-i\gamma\hat{J}_z}. \tag{2}$$

Finally, the "collective amplitudes" $f^I_\sigma(q_{20})$ as well as the energies of the AMP-GCM states $\left|\Phi^I_\sigma\right\rangle$ are obtained through the solution of the Hill-Wheeler (HW) equation

$$\int \mathrm{d}q'_{20} \mathcal{H}^I(q_{20}, q'_{20}) f^I_\sigma(q'_{20}) = E^I_\sigma \int \mathrm{d}q'_{20} \mathcal{N}^I(q_{20}, q'_{20}) f^I_\sigma(q'_{20}) \tag{3}$$

which is given in terms of the projected norm

$$\mathcal{N}^I(q_{20}, q'_{20}) = \langle\varphi(q_{20})| \hat{P}^I_{00} |\varphi(q'_{20})\rangle \tag{4}$$

and the projected Hamiltonian kernel

$$\mathcal{H}^I(q_{20}, q'_{20}) = \langle\varphi(q_{20})| \hat{H}\hat{P}^I_{00} |\varphi(q'_{20})\rangle . \tag{5}$$

As the generating states $\hat{P}^I_{00} |\varphi(q_{20})\rangle$ are not orthogonal, the "collective amplitudes" $f^I_\sigma(q_{20})$ cannot be interpreted as probability amplitudes. Instead, one usually introduce [24] the "collective" wave functions

$$g^I_\sigma(q_{20}) = \int \mathrm{d}q'_{20} f^I_\sigma(q'_{20}) \left(\mathcal{N}^I(q_{20}, q'_{20})^*\right)^{1/2} \tag{6}$$

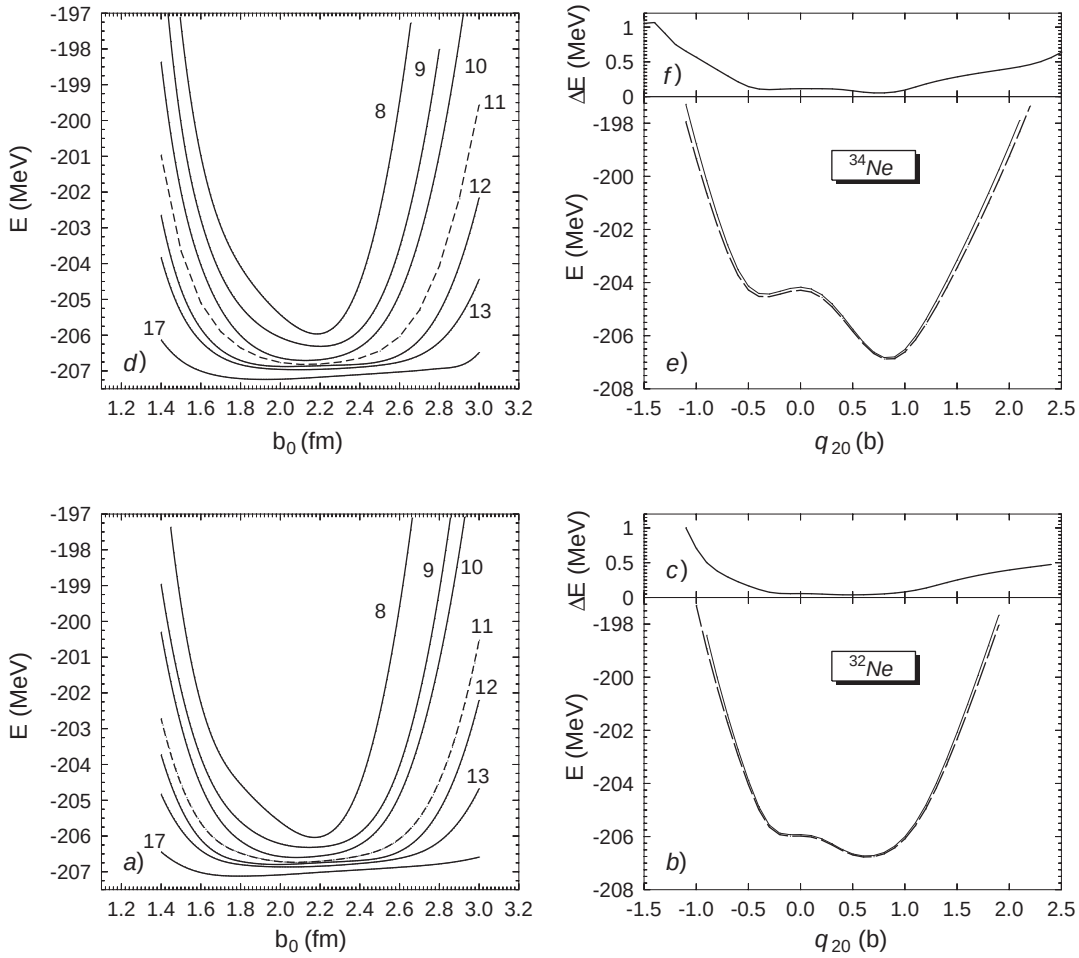

Fig. 1. In panels a) and d) the ground-state HFB energies of ^{32,34}Ne are plotted as functions of the HO length b_0 ($b_\perp = b_z = b_0$) for the $N_{\rm shell} = 8, 9, 10, 11, 12, 13$ and 17 bases. The curve corresponding to the basis used in the present work ($N_{\rm shell} = 11$) is plotted as a dashed line. In panels b) and e) the HFB energies of ^{32,34}Ne computed with $b_0 = 2.1$ fm and $N_{\rm shell} = 11$ (full line) and $N_{\rm shell} = 12$ (dashed line) are plotted as functions of the quadrupole moment. In panels c) and f), the energy differences between $N_{\rm shell} = 11$ and $N_{\rm shell} = 12$ calculations are plotted as functions of the quadrupole moment.

which are orthonormal $\int {\rm d}q_{20} g^{I\,*}_{\sigma}(q_{20}) g^{I'}_{\sigma'}(q_{20}) = \delta_{I,I'}\delta_{\sigma,\sigma'}$ and therefore their module squared has the meaning of a probability.

In order to readjust the particle number on the average for the projected wave functions the Hamiltonian in eq. (5) has been replaced by $\hat{H}' = \hat{H} - \lambda_{\rm n}(\hat{N} - N_0) - \lambda_{\rm p}(\hat{Z} - Z_0)$ where $\lambda_{\rm n}$ and $\lambda_{\rm p}$ are chemical potential parameters (see ref. [25], and references therein).

The $B(E2)$ transition probabilities are computed using the AMP-GCM wave functions

$$B(E2, I_{\rm i} \rightarrow I_{\rm f}) = \frac{e^2}{2I_{\rm i}+1} \times \left| \int {\rm d}q_{20} {\rm d}q'_{20} f^{I_{\rm f}\,*}_{\sigma_{\rm f}}(q'_{20}) \langle I_{\rm f} q'_{20} \mid\mid \hat{Q}_2 \mid\mid I_{\rm i} q_{20} \rangle f^{I_{\rm i}}_{\sigma_{\rm i}}(q_{20}) \right|^2 \quad (7)$$

with

$$\frac{\langle I_{\rm f} q'_{20} \mid\mid \hat{Q}_2 \mid\mid I_{\rm i} q_{20} \rangle}{(2I_{\rm i}+1)(2I_{\rm f}+1)} = \sum_{\mu} \begin{pmatrix} I_{\rm i} & 2 & I_{\rm f} \\ -\mu & \mu & 0 \end{pmatrix} \times \int_0^{\frac{\pi}{2}} {\rm d}\beta \sin\beta {\rm d}^{I_{\rm i}}_{-\mu,0}(\beta) \langle \varphi(q'_{20}) \mid \hat{Q}_{2\mu} e^{-i\beta \hat{J}_y} \mid \varphi(q_{20}) \rangle \,,$$

where the indices i and f stand for the initial and final states and $\hat{Q}_{2\mu}$ are the charge quadrupole moment operators. As we are using the full configuration space no effective charges are needed. Further details on the computational procedure can be found in ref. [25].

3 Discussion of the results

3.1 Mean-field approximation

Before discussing the mean-field results, the convergence of our calculations with the size of the Harmonic-Oscillator (HO) basis used to discretize the HFB equation has to be tested as we are dealing with near-drip-line nuclei like ^{32,34}Ne. First, one should note that, due to the proximity of the drip line, the full HFB approximation

must be used [26,27]. It is also evident that absolute convergence for the binding energies can only be attained for HO basis with an infinity number of shells ($N_{\rm shell}$). However, it is expected that other physical observables like excitation energies, transition probabilities, etc. can be accurately described with a finite number of shells.

In order to determine how many shells are needed for an accurate description of the physical observables we have first studied the behavior of the HFB energy as a function of the oscillator length parameter b_0 ($b_\perp = b_z = b_0$) and the number of shells for the nuclei ^{32}Ne and ^{34}Ne. The results are plotted in panels a) and d) of fig. 1. As expected the curves become more and more flat for increasing values of $N_{\rm shell}$ and already the $N_{\rm shell} = 17$ basis can be considered as a good approximation for an infinite basis in both isotopes as the dependence of the energies on the oscillator length is very weak for a wide range of b_0 values. However, $N_{\rm shell} = 17$ makes the HO basis too big for our purposes as we have to evaluate the AMP-GCM Hamiltonian kernel which is a quantity requiring two orders of magnitude more computing time than the whole HFB calculation. We have found that $N_{\rm shell} = 11$ is a good compromise between accuracy and computing time as the energy still shows a weak dependence on the oscillator length around the minima located at $b_0 = 2.1$ fm for both ^{32}Ne (panel a)) and ^{34}Ne (panel d)). As an example of the adequacy of the $N_{\rm shell} = 11$ calculations let us consider the two-neutron separation energy of ^{34}Ne. The $N_{\rm shell} = 17$ ground-state energies for ^{32}Ne and ^{34}Ne are 403 keV and 420 keV lower than the $N_{\rm shell} = 11$ energies implying that the two-neutron separation energy of ^{34}Ne computed with $N_{\rm shell} = 11$ differs by 17 keV from the one computed with $N_{\rm shell} = 17$.

In order to study the suitability of the $N_{\rm shell} = 11$ basis for other nuclear properties we have performed calculations with $N_{\rm shell} = 12$. The mean-field results for both calculations are compared on the right-hand side panels of fig. 1. In panels b) and e) the energy landscapes of ^{32}Ne and ^{34}Ne are shown as a function of the quadrupole moment for the $N_{\rm shell} = 11$ and $N_{\rm shell} = 12$ calculations. In the upper panels c) and f) we have represented the energy differences between both calculations. The conclusion is that in the region -0.7 b $\leq q_{20} \leq 1.2$ b the shape of the energy landscapes do not change much when the basis is increased from $N_{\rm shell} = 11$ to $N_{\rm shell} = 12$. As we will see later on, this is the range of q_{20} values where the collective dynamics is concentrated and therefore it is not expected to find significant differences between the $N_{\rm shell} = 11$ and $N_{\rm shell} = 12$ results.

In fig. 2 the mean-field potential energy surfaces (MFPES) are plotted as a function of the axially symmetric quadrupole moment q_{20} for the even-even neon isotopes $^{20-34}$Ne. The MFPES shown do not include the Coulomb exchange energy and they have been shifted to accommodate them in a single plot (see figure caption).

Both ^{20}Ne and ^{22}Ne are prolate deformed in their ground states. In ^{20}Ne the prolate ground state corresponds to $q_{20} = 0.4$ b ($\beta_2 = 0.37$) and an oblate local minimum also appears at $q_{20} = -0.1$ b ($\beta_2 = -0.09$) with

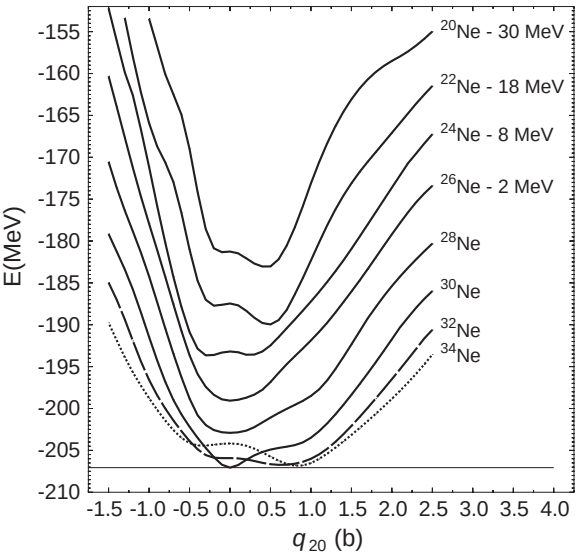

Fig. 2. Mean-field potential energy surfaces for the considered neon isotopes, plotted as a function of the axially symmetric quadrupole moment. The curves have been shifted to show them in a single plot. The corresponding energy shifts are given in the plot.

an excitation energy of 1.71 MeV. In the case of ^{22}Ne the ground state corresponds to $q_{20} = 0.5$ b ($\beta_2 = 0.40$) and another local minimum is found at $q_{20} = -0.2$ b ($\beta_2 = -0.17$) with an excitation energy of 2.24 MeV. The nucleus ^{24}Ne is a clear example, in the considered isotopic chain, of very strong shape coexistence since, while the oblate ground state is locate at $q_{20} = -0.3$ b ($\beta_2 = -0.22$), a prolate isomeric state is also found at $q_{20} = 0.2$ b ($\beta_2 = 0.15$) with an excitation energy with respect to the oblate ground state of 77 keV. On the other hand, the nuclei $^{26-30}$Ne show spherical ground states indicating that the $N = 20$ shell closure is preserved at the mean-field level. The MFPES of both ^{26,28}Ne are particularly flat around their spherical ground states. In the nucleus ^{30}Ne we obtain a prolate shoulder at $q_{20} = 0.8$ b ($\beta_2 = 0.37$) at an excitation energy of 2.70 MeV with respect to the spherical ground state. This prolate shoulder is around 1 MeV higher than the one found in similar HFB calculations in ^{32}Mg (see for example [15]). In the drip line systems ^{32}Ne and ^{34}Ne, prolate deformed ground states are found. The ground states have $q_{20} = 0.6$ b ($\beta_2 = 0.26$) and $q_{20} = 0.8$ b ($\beta_2 = 0.31$), respectively. In addition, an oblate isomeric state is found in ^{34}Ne at $q_{20} = -0.3$ b ($\beta_2 = -0.12$) with an excitation energy of 2.39 MeV with respect to the prolate ground state.

Another interesting point concerns the stability of the Ne isotopes against neutron emission. From the absolute minimum of the MFPES depicted in fig. 2 (the one of ^{30}Ne is marked with a horizontal line) it can be deduced that ^{32}Ne is not stable against two-neutron emission. This is in clear contradiction with the experimental results as they indicate that ^{32}Ne is indeed stable against two-neutron emission [28–30]. On the other hand, the nucleus ^{34}Ne is

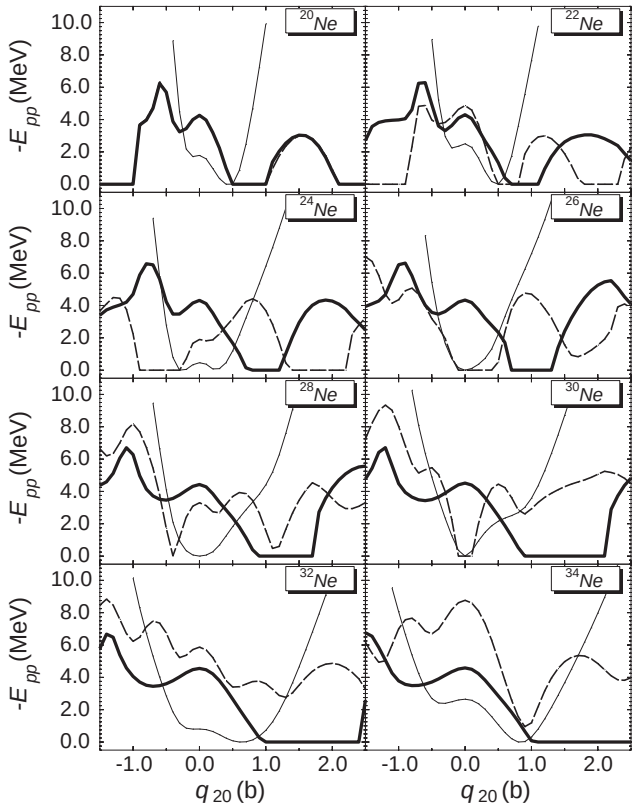

Fig. 3. In each panel, proton (thick full lines) and neutron (thick dashed lines) particle-particle energies $-E_{\rm pp}$ are depicted as a function of the quadrupole moment. Also the energy differences $E_{\rm HFB}(q_{20}) - E_{\rm g.s.}$, where $E_{\rm g.s.}$ corresponds to the ground-state HFB configuration, are plotted as thin full lines.

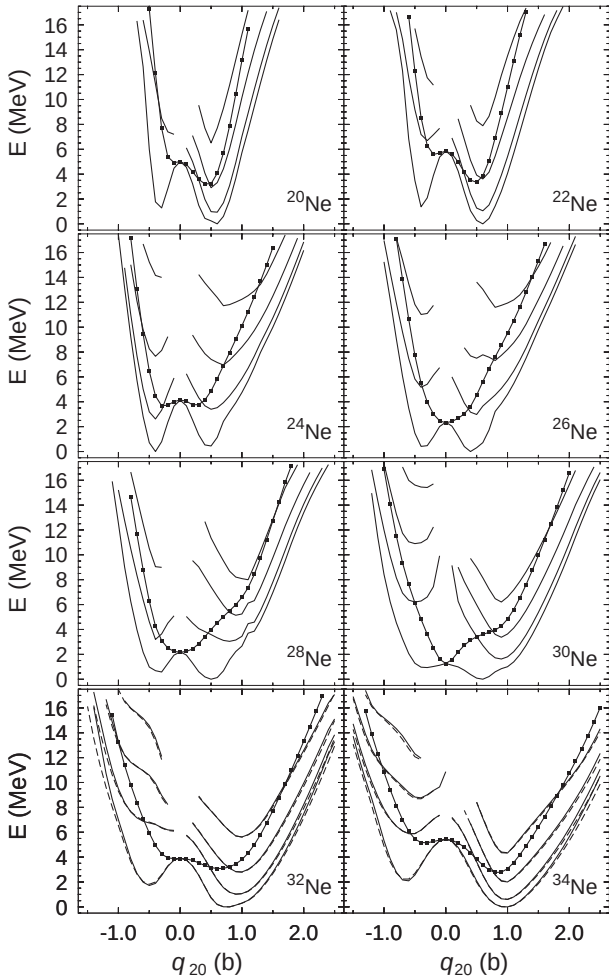

Fig. 4. Angular momentum projected potential energy surfaces (full lines) for the nuclei $^{20-34}$Ne and for the spin values $I^\pi = 0^+, 2^+, 4^+$and 6^+, plotted as a function of the axially symmetric quadrupole moment q_{20}. The mean-field potential energy surfaces are also plotted as lines with boxes. In each nucleus, the energies are referred to the energy of the $I^\pi = 0^+$ ground state. For the nuclei $^{32-34}$Ne we have also included (dashed lines) the projected results corresponding to the calculation with $N_{\rm shell} = 12$.

slightly stable against two-neutron emission, but it is not against four-neutron emission.

In fig. 3 the proton and neutron particle-particle correlation energies $-E_{\rm pp} = \frac{1}{2}{\rm Tr}\,(\Delta\kappa^*)$, which are commonly used to discuss pairing correlations (see for example refs. [20,31]), are plotted as a function of the quadrupole deformation for all the isotopes considered. The evolution of the particle-particle correlation energies is well correlated with the structures found in the MFPES. Non-zero proton pairing correlations are found in all the spherical or oblate minima. In addition, sizeable neutron pairing correlations are found in ^{20,22}Ne and ^{32,34}Ne for the spherical and the oblate minima. Vanishing proton pairing correlations are found in the prolate side in a window starting at 0.5 b and ending in 1.0 b in ^{20}Ne. For the other isotopes the starting and ending points increase with the neutron number. Neutron pairing correlations vanish in the ground states of both ^{26}Ne and ^{30}Ne. In the later case this is a consequence of the $N = 20$ shell closure found at the mean-field level.

It should be stressed here that the unphysical collapse of pairing correlations found in fig. 3 is an indication that one should also consider in these isotopes dynamical pairing correlations and their coupling to the quadrupole degree of freedom in the scope of a formalism beyond the mean field in order to treat them in an equal footing. However, this multidimensional configuration mixing calculation is a cumbersome task with the present-day computational facilities.

3.2 Correlations beyond the mean field: angular momentum projection

Before considering the full AMP-GCM, it is instructive to look into the Angular Momentum Projected Energy Surfaces (AMPPES) defined as

$$E^I(q_{20}) = \frac{\mathcal{H}^I(q_{20}, q_{20})}{\mathcal{N}^I(q_{20}, q_{20})} \tag{8}$$

and shown in fig. 4 for the nuclei $^{20-34}$Ne and $I = 0$, 2, 4, and 6. The corresponding mean-field energy landscapes

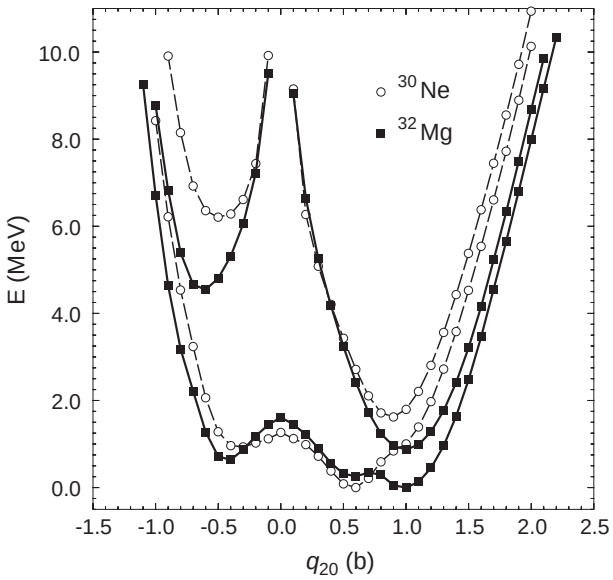

Fig. 5. A comparison of the angular momentum projected energies of the ^{30}Ne and ^{32}Mg nuclei as functions of the quadrupole moment for $I^\pi = 0^+$and 2^+ (referred to the $I^\pi = 0^+$ absolute minimum in each nucleus).

(lines with boxes) are also included for comparison. For details on the missing points in the $I = 2$, 4 and 6 curves refer to [25]. The most remarkable fact about fig. 4 is how strongly the restoration of the rotational symmetry modifies the mean-field picture of the $I = 0$ configurations. Contrary to the mean-field case, two minima, one prolate and the other oblate, are obtained for all the neon isotopes for $I^\pi = 0^+$. The prolate minimum is, with the exception of ^{24}Ne, the absolute minimum in all the isotopes considered. For increasing spin values either the energy difference between the prolate and oblate minima increases or the oblate minimum is washed out.

The nucleus ^{24}Ne, with its $I^\pi = 0^+$ oblate ground state is the exception in all the neon isotopes studied. The orbital responsible for such an oblate minimum is the neutron $d_{\frac{5}{2}}$ orbital which becomes fully occupied in this nucleus and favors oblate deformations. The absolute minimum remains oblate for $I^\pi = 2^+$ but already at $I^\pi = 4^+$ it becomes prolate deformed.

In addition, shape coexistence is expected in the nuclei ^{26}Ne, ^{28}Ne and ^{30}Ne as their $I^\pi = 0^+$ prolate and oblate minima are very close in energy (414, 577 and 936 keV, respectively). These minima are separated by barriers which are 2.4, 2.2 and 1.3 MeV high, respectively.

Finally, it is also worth comparing the intrinsic quadrupole deformation of the ground state of ^{30}Ne with the one of ^{32}Mg [14]. In fig. 5 we have plotted the $I^\pi = 0^+$ and 2^+ AMPPES for both ^{30}Ne and ^{32}Mg. From this plot we conclude that the absolute minimum of the $I^\pi = 0^+$ AMPPES in ^{30}Ne has half the deformation of the corresponding minimum in ^{32}Mg. On the other hand, the $I^\pi = 2^+$ deformations are practically identical. From this results one may expect, as is the case, very similar spectroscopic quadrupole moments for the first 2^+ states in

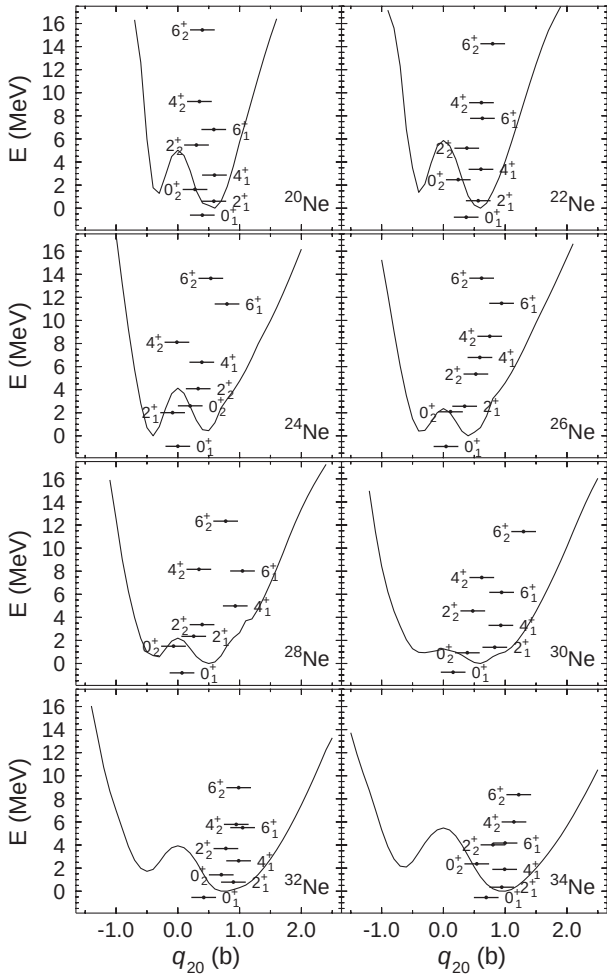

Fig. 6. Band diagrams for the nuclei $^{20-34}$Ne obtained by solving the Hill-Wheeler equation of the AMP-GCM. The $I = 0$ AMPPES are also plotted to guide the eye. See text for further details.

^{30}Ne and ^{32}Mg and a reduction of the $B(E2)$ transition probability in ^{30}Ne as compared to the one of ^{32}Mg.

3.3 Correlations beyond the mean field: angular momentum projection and configuration mixing

The AMPPES of the previous subsection show for some nuclei and/or some spin values the phenomenon of shape coexistence and therefore configuration mixing has to be considered in order to gain a better understanding of the structure of these states. We have considered configuration mixing in the framework of the Angular Momentum Projected Generator Coordinate Method (AMP-GCM) described in sect. 2. The intrinsic axial quadrupole moment q_{20} with values in the range -1.5 b $\leq q_{20} \leq 2.5$ b and with a mesh size Δq_{20} of 10 fm^2 has been chosen as generating coordinate.

In fig. 6 we have plotted the AMP-GCM energies E^I_σ obtained by solving the Hill-Wheeler equation and placed them along the q_{20}-axis according to their "average

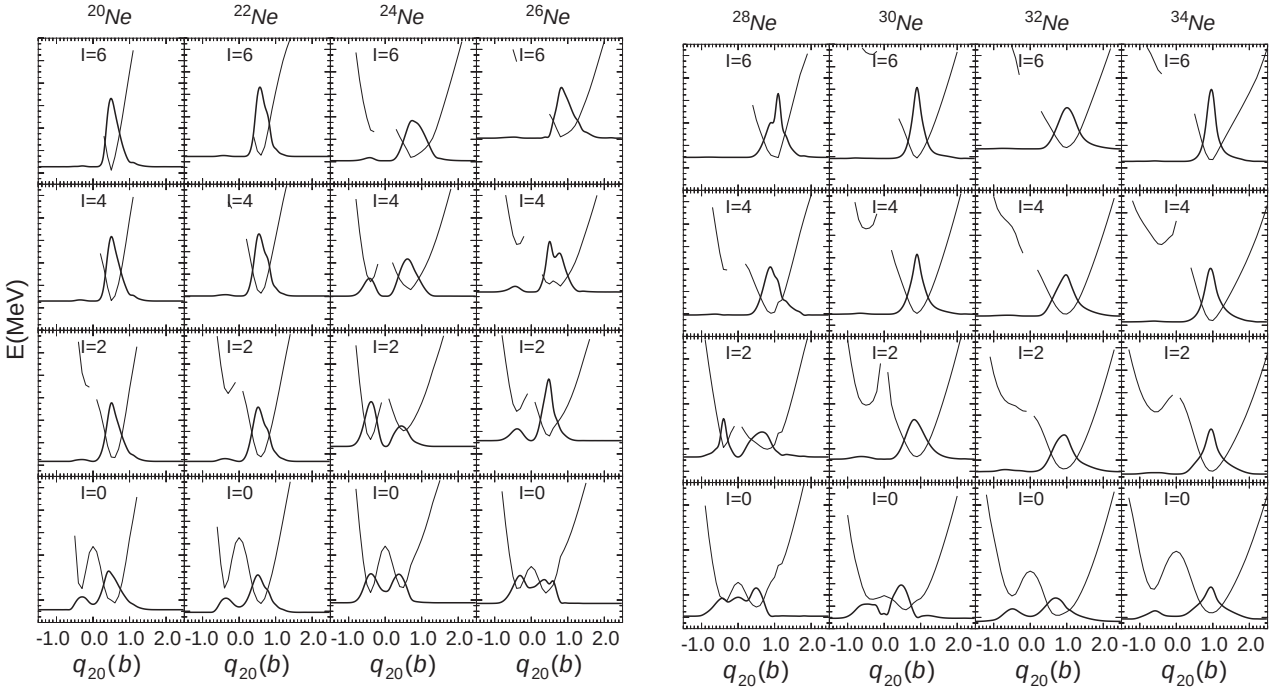

Fig. 7. Collective wave functions squared for the ground states ($\sigma = 1$) and the spin values $I^\pi = 0^+, 2^+, 4^+$and 6^+ of the nuclei $^{20-34}$Ne. The corresponding projected energy curve is also plotted for each spin value. The y-axis scales are in energy units and always span an energy interval of 13 MeV (minor ticks are 0.5 MeV apart). The collective wave functions have also been plotted against the energy scale after proper scaling and shifting, that is, the quantity $E^I_\sigma + 15\times \mid g^I_\sigma(q_{20}) \mid^2$ is the one actually plotted. With this choice of the scales we can read from the figure the energy gain due to quadrupole fluctuations by considering the position of the wave functions' tail relative to the projected curve.

intrinsic quadrupole moment" defined as

$$\overline{q}^{I,\sigma}_{20} = \int \mathrm{d}q_{20} \mid g^I_\sigma(q_{20}) \mid^2 q_{20}\,. \tag{9}$$

In this figure we have also plotted the $I^\pi = 0^+$ AMPPES to guide the eye. The first noticeable fact is that the correlated 0^+ ground states have a lower energy than the absolute minimum of the corresponding AMPPES. This energy gain due to the quadrupole correlations increases the binding energies and can be relevant for a proper description of the two-neutron separation energies. The second prominent feature is that configuration mixing decreases the deformation of the 0^+_1 ground states with respect to the minimum of the AMPPES. The ground states of the nuclei ^{24}Ne and ^{26}Ne become spherical, whereas the ones of ^{28}Ne and ^{30}Ne become weakly deformed. The other nuclei remain well deformed in their ground states and develop a rather well-defined rotational band up to the maximum spin considered for $\sigma = 1$. In addition, a well-defined rotational band is obtained for $I \geq 2$ in ^{30}Ne. On the other hand, the excited states ($\sigma = 2$) only show a rotational-band pattern for those nuclei well deformed in their ground state. Another interesting point concerns the energy gain due to configuration mixing of the ground state: it is 0.6 MeV for ^{20}Ne, increases up to 0.9 MeV for ^{24}Ne and ^{26}Ne and then monotonically decreases up to 0.55 MeV in ^{34}Ne. The energy gain is correlated with the shape of the AMPPES for $I = 0$, namely, if the AMPPES shows a well-defined minimum the energy gain is smaller than in the case where the minimum is broader.

To gain a deeper insight into the intrinsic structure of the AMP-GCM states the ground-band ($\sigma = 1$) collective wave functions squared $\mid g^I_\sigma(q_{20}) \mid^2$ are plotted in fig. 7 along with the corresponding AMPPES. For ^{20}Ne and ^{22}Ne the ground-state collective wave functions are well inside the prolate wells indicating that both systems are dominated by prolate deformations in the considered spin range. The average deformation values are 0.39 b, 0.58 b, 0.59 b and 0.58 b for the 0^+_1, 2^+_1, 4^+_1 and 6^+_1 states in ^{20}Ne, while the corresponding values in ^{22}Ne are 0.39 b, 0.56 b, 0.61 b and 0.63 b. In the nucleus ^{24}Ne, the configuration mixing calculation provides a spherical 0^+_1 instead of the oblate absolute minimum found in its AMPPES. An almost spherical 2^+_1 state ($\overline{q}^{I=2,\sigma=1}_{20} = -0.08$ b) is also found in this nucleus. On the other hand, a band crossing takes place for the state 4^+_1 and the collective wave function becomes prolate deformed with $\overline{q}^{I=4,\sigma=1}_{20} = 0.39$ b and $\overline{q}^{I=6,\sigma=1}_{20} = 0.79$ b. Similar results have recently been found [25] in the $N = 14$ system ^{26}Mg. The experimental spectroscopic quadrupole moment of the lowest 2^+ state in ^{26}Mg is -13.5 $e$fm^2 [32] indicating that this is a prolate state. However, the low excitation energy of the 0^+_2 in ^{26}Mg (3.588 MeV) compared with the same quantity in ^{24}Mg (6.432 MeV) clearly indicates strong shape coexistence between oblate and prolate solutions. Unlike ^{26}Mg, there is not experimental information concerning the

spectroscopic quadrupole moment of the lowest 2^+ state in ^{24}Ne but again the experimental excitation energies of the 0_2^+ in ^{24}Ne and ^{26}Ne (4.764 MeV and 3.691 MeV, respectively) are significantly lower than the 6.235 MeV measured in ^{22}Ne [32,33] pointing towards a strong shape coexistence in the ground state of the former nuclei. Our results predict a strong shape coexistence for the 0_1^+ and 2_1^+ states in ^{24}Ne as well as for the 0_1^+ states in ^{26}Ne and ^{28}Ne that manifest itself in the 0_2^+ excitation energies of 3.509 and 3.005 MeV for ^{24,26}Ne, respectively.

The 0_1^+ wave functions in both ^{26}Ne and ^{28}Ne show a great admixture of prolate and oblate configurations that leads to spherical ground states on the average. On the other hand, for $I^\pi \geq 2^+$ the collective wave functions in these two nuclei become prolate deformed with deformation values of 0.34 b, 0.59 b and 0.94 b for the states 2_1^+, 4_1^+ and 6_1^+ in ^{26}Ne, while the corresponding values in ^{28}Ne are 0.26 b, 0.93 b and 1.04 b. Our results do not fully support the suggestion of [19] concerning the magicity of $N = 16$ in neutron-rich light nuclei. It is true that ^{26}Ne has a spherical ground state, but the deformation of the 2_1^+ is too strong as to be considered a vibrational state. Similar results are also found in ref. [25] for the $N = 16$ nucleus ^{28}Mg.

The 0_1^+ wave function in ^{30}Ne also shows a significant admixture of the oblate and prolate configurations and, as a consequence, the deformation in the ground state is reduced to 0.16 b that represents one third of the value corresponding to the absolute minimum in the $I^\pi = 0^+$ AMPPES. This clearly shows that, as in ^{32}Mg [13,15,25], the deformation effects in ^{30}Ne are the result of a subtle balance between the zero-point corrections associated with the restoration of the rotational symmetry and the fluctuations in the collective parameters (in our case the axially symmetric quadrupole moment). From the comparison with the value of $\overline{q}_{20}^{I=0,\sigma=1} = 0.43$ b already found [15, 25] in ^{32}Mg we conclude that dynamical deformation effects are strongly suppressed in ^{30}Ne as could have been forecasted from the different AMPPES topology we have already seen in fig. 5. On the other hand, the 2_1^+, 4_1^+ and 6_1^+ wave functions in ^{30}Ne are inside the prolate wells and the average deformations of 0.83 b, 0.93 b and 0.94 b are very close to the ones found in ^{32}Mg.

In both ^{32}Ne and ^{34}Ne, the ground-state collective wave functions become prolate. The dynamical deformation values for the 0_1^+, 2_1^+, 4_1^+ and 6_1^+ in ^{32}Ne are 0.42 b, 0.90 b, 0.98 b, 1.05 b, while the corresponding values in ^{32}Ne are 0.69 b, 0.94 b, 0.99 b and 1.0 b. All these values show the stability of deformation effects in neon isotopes as we move towards the drip line.

Here, we will make a few comments on the AMP-GCM results in the nuclei ^{32}Ne and ^{34}Ne when the basis is increased from $N_{\rm shell} = 11$ to $N_{\rm shell} = 12$. The effect on the projected energy landscapes can be seen in the corresponding panels of fig. 4 where $N_{\rm shell} = 12$ curves are plotted as dashed lines. The results with $N_{\rm shell} = 12$ and $N_{\rm shell} = 11$ only show very small differences at large absolute values of q_{20}. On the other hand, in the region of physical significance (-0.7 b $\leq q_{20} \leq 1.2$ b) the results are practically indistinguishable. Since this range of q_{20} values is the one where the collective dynamics is concentrated (*i.e*, the tails of the collective wave functions go to zero outside this range) we do not expect big changes in the excitation energies. For the ^{32}Ne nucleus, it turns out that the excitation energies of all the members of the ground-state rotational band obtained in the $N_{\rm shell} = 12$ calculation are around 7 keV higher than the ones in the $N_{\rm shell} = 11$ case, *i.e.*, only the 0_1^+ state has been pushed down. For ^{34}Ne the average shift is 6 keV. As a consequence, the transition gamma-ray energies remain unaltered by the increase of the basis size. On the other hand, the excitation energies (with respect to the true ground state) of the members of the excited rotational band decrease on the average 40 keV in ^{32}Ne and 32 keV in ^{34}Ne and, therefore, as in the previous case, the intra-band gamma-ray energies remain the same. From these results we conclude that our calculations are well converged in terms of the basis size.

Table 1. Ground-state spectroscopic quadrupole moments $Q^{\rm spec}(I, \sigma = 1)$ in $e$fm^2 for $I^\pi = 2^+$, 4^+ and 6^+ in the nuclei $^{20-34}$Ne. Experimental data [32,34] are shown in boldface, whereas Shell Model results [35,36] are shown in brackets. For details see the main text.

I	^{20}Ne	^{22}Ne	^{24}Ne	^{26}Ne
2	-16.75	-14.64	2.02	-7.88
	$\mathbf{-23}$	$\mathbf{-17}$	(-2.77)	(-10.56)
4	-21.52	-21.03	-11.62	-16.98
6	-23.29	-23.01	-27.01	-28.78
I	^{28}Ne	^{30}Ne	^{32}Ne	^{34}Ne
2	-10.05	-15.80	-17.49	-15.81
	(-17.8)	(-16.40)	(-20.00)	(-16.56)
4	-26.11	-22.21	-22.25	-21.38
6	-29.83	-24.82	-26.23	-23.52

Coming back to the discussion of our results, in table 1 we present our results for the ground-band spectroscopic quadrupole moments. A very good agreement is observed between the calculated spectroscopic values of the 2_1^+ states in ^{20}Ne and ^{22}Ne and the experimental values (shown in boldface) for these nuclei which are -23 $e$fm^2 [34] and -17 $e$fm^2 [32], respectively. In addition, our results are consistent with the Shell Model predictions (shown in brackets) for the spectroscopic quadrupole moments of the 2_1^+ states [35,36]. Obviously, the discrepancies are larger for the shape coexistent nuclei $^{24-28}$Ne, It is also worth mentioning here that the value obtained for the spectroscopic quadrupole moment of the 2_1^+ state in ^{30}Ne (-15.80 $e$fm^2) is only slightly smaller than the similar quantity in ^{32}Mg (-19.50 $e$fm^2).

In fig. 8 we compare the results of the AMP-GCM two-neutron separation energies $S_{2N} = E_{0_1^+}(N-2) - E_{0_1^+}(N)$ with the corresponding mean-field results (see sect. 3.1) and also with the available experimental values taken from refs. [37,38]. The AMP-GCM improves the S_{2N} of ^{26}Ne as compared to the mean-field results and also makes the

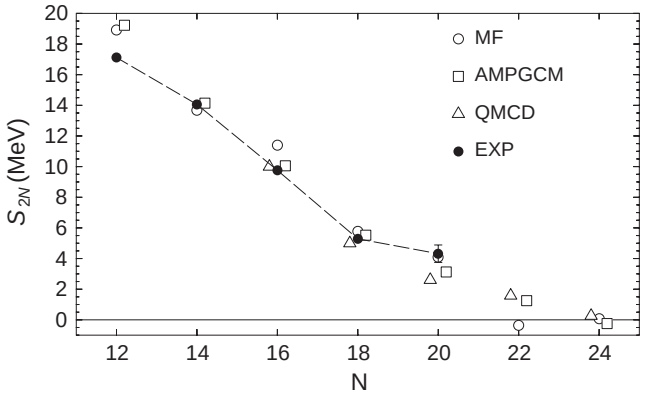

Fig. 8. The two-neutron separation energies obtained with the different approximations considered in this paper are compared to experimental values taken from refs. [37,38] and the QMCD results of refs. [39,40].

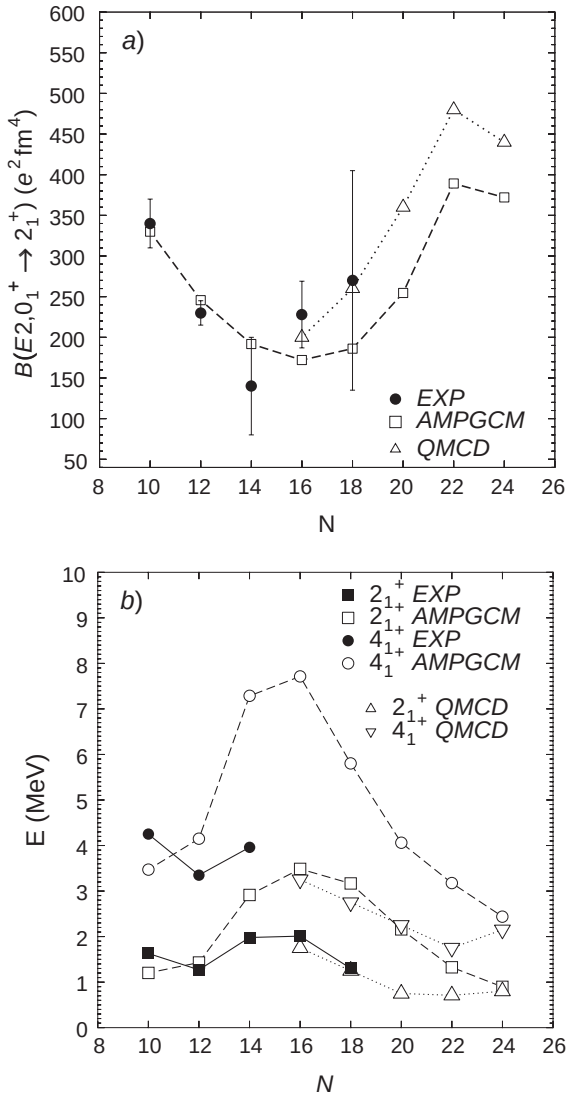

Fig. 9. In panel a) the experimental values [32,33,41–44] of the $B(E2,0_1^+ \rightarrow 2_1^+)$ transition probabilities are compared to our predictions and other theoretical results [39,40]. In panel b) the same comparison is made for the 2_1^+ and 4_1^+ excitation energies.

nucleus ^{32}Ne bound (unlike the mean-field prediction) in good agreement with the experimental results [28–30]. On the other hand, the nucleus ^{34}Ne becomes unstable against two-neutron emission in the AMP-GCM approach. Our results are very similar to the ones predicted in the framework of the QMCD [39,40] specially around $N = 20$ but we differ in the prediction concerning ^{34}Ne. Finally, it is worth mentioning that the AMP-GCM binding energy is the sum of the mean-field binding energy of the intrinsic state plus the energy gain due to the restoration of the rotational symmetry plus the energy gain due to the configuration mixing. Therefore, the differences in S_{2N} obtained in the AMP-GCM and the mean field are due to the last two contributions. The analysis of those contributions shows that the rotational energy correction is the main responsible for the differences observed in S_{2N} and, therefore, is the ingredient needed to make ^{32}Ne stable.

In fig. 9 the excitation energies of the 2_1^+ and 4_1^+ states and the $B(E2,0_1^+ \rightarrow 2_1^+)$ transition probabilities obtained in the AMP-GCM are compared with the available experimental values and also with the predictions of the QMCD [39,40]. Concerning the $B(E2,0_1^+ \rightarrow 2_1^+)$ transition probabilities we clearly see, from panel a), that the agreement with the available experimental data [32,33, 41–44] is rather satisfactory and in most cases (with the exception of ^{26}Ne where our prediction appears a little bit low) our results stay within the experimental error bars. On the other hand, our results are also consistent with the predictions of the QMCD [39,40]. Our results, although not as good as the QMCD ones, are very satisfactory considering that the parameters of the Gogny force have not been fitted to the region and/or the physics of quadrupole collectivity and also that no effective charges have been used in our calculations of the transition probabilities.

Our results for the 2_1^+ excitation energies agree well with the experiment in ^{20}Ne and ^{22}Ne [32,33] and also with the theoretical result of Otsuka in ^{34}Ne. For the other isotopes our 2^+ excitation energies are always higher than experiment and the QMCD predictions. The same happens for the 4^+ excitation energies. The disagreement between our results and the experiment (or the QMCD predictions) can be attributed to the fact that the nuclei involved are nice examples of shape coexistence. In the presence of shape coexistence the quadrupole degree of freedom probably is not enough to describe accurately the observables and other degrees of freedom like triaxiality or pairing fluctuations should be included. However, and based on the nice agreement between our electromagnetic transition probabilities and the experimental ones, we can conclude that the quadrupole degree of freedom is the main ingredient in the physical picture of the neutron-rich neon isotopes.

4 Conclusions

We have performed Angular Momentum Projected Generator Coordinate Method calculations with the Gogny interaction D1S and the mass quadrupole moment as generating coordinate in order to describe quadrupole

collectivity in the even-even nuclei $^{20-34}$Ne. The lighter isotopes ^{20}Ne and ^{22}Ne as well as the heavier ones ^{32}Ne and ^{34}Ne are well deformed in their ground states, whereas the other isotopes are either spherical (^{24}Ne and ^{26}Ne) or slightly deformed like ^{28}Ne and ^{30}Ne. The later isotope is less deformed in its ground state than its isotone ^{32}Mg. The two-neutron separation energies compare well with experimental data and show that ^{32}Ne is bound. Moreover, the $B(E2)$ transition probabilities from the ground state to the 2^+ state are well reproduced in all the cases. Only the 2^+ excitation energies result to be too high as compared to the experiment for the shape coexistent isotopes.

This work has been supported in part by the DGI, Ministerio de Ciencia y Tecnología (Spain) under project BFM2001-0184.

References

1. C. Thibault, R. Kapisch, C. Rigaud, A.M. Poskanzer, R. Prieels, L. Lessard, W. Reisdorf, Phys. Rev. C **12**, 644 (1975).
2. F. Touchard, J.M. Serre, S. Büttgenbach, P. Guimbal, R. Kapisch, M. De Saint-Simon, C. Thibault, H.T. Duong, P. Juncar, S. Liberman, J. Pinard, J.L. Vialle, Phys. Rev. C **25**, 2756 (1982).
3. X. Campi, H. Flocard, A.K. Kerman, S. Koonin, Nucl. Phys. A **251**, 193 (1975).
4. A. Poves, J. Retamosa, Phys. Lett. B **184**, 311 (1987).
5. E.K. Warburton, J.A. Becker, B.A. Brown, Phys. Rev. C **41**, 1147 (1990).
6. D. Guillemaud-Mueller, C. Détraz, M. Langevin, F. Naulin, M. De Saint-Simon, C. Thibault, F. Touchard, M. Epherre, Nucl. Phys. A **426**, 37 (1984).
7. G. Klotz, P. Baumann, M. Bounajma, A. Huck, A. Knipper, G. Walter, G. Marguier, C. Richard-Serre, A. Poves, J. Retamosa, Phys. Rev. C **47**, 2502 (1993).
8. T. Motobayashi, Y. Ikeda, Y. Ando, K. Ieki, M. Inoue, N. Iwasa, T. Kikuchi, M. Kurokawa, S. Moriya, S. Ogawa, H. Murakami, S. Shimoura, Y. Yanagisawa, T. Nakamura, Y. Watanabe, M. Ishiara, T. Teranishi, H. Okuno, R.F. Casten, Phys. Lett. B **346**, 9 (1995).
9. K. Yoneda, H. Sakurai, T. Gomi, T. Motobayashi, N. Aoi, N. Fukuda, U. Futakami, Z. Gacsi, Y. Higurashi, N. Imai, N. Iwasa, H. Iwasaki, T. Kubo, M. Kunibu, M. Kurokawa, Z. Liu, T. Minemura, A. Saito, M. Serata, S. Shimoura, S. Takeuchi, Y. X. Watanabe, K. Yamada, Y. Yanagisawa, K. Yogo, A. Yoshida, M. Ishihara, Phys. Lett. B **499**, 233 (2001).
10. H. Iwasaki, T. Motobayashi, H. Sakurai, K. Yoneda, T. Gomi, N. Aoi, N. Fukuda, Zs. Fülöp, U. Futakami, Z. Gacsi, Y. Higurashi, N. Imai, N. Iwasa, T. Kubo, M. Kunibu, M. Kurokawa, Z. Liu, T. Minemura, A. Saito, M. Serata, S. Shimoura, S. Takeuchi, Y.X. Watanabe, K. Yamada, Y. Yanagisawa, K. Yogo, M. Ishihara, Phys. Lett. B **522**, 227 (2001).
11. J.F. Berger, J.P. Delaroche, M. Girod, S. Péru, J. Libert, I. Deloncle, Inst. Phys. Conf. Ser. **132**, 487 (1993).
12. P.-G. Reinhard, D.J. Dean, W. Nazarewicz, J. Dobaczewski, J.A. Maruhn, M.R. Strayer, Phys. Rev. C **60**, 014316 (1999).
13. P.-H. Heenen, P. Bonche, S. Cwiok, W. Nazarewicz, A. Valor, RIKEN Rev. **26**, 31 (2000).
14. R. Rodríguez-Guzmán, J.L. Egido, L.M. Robledo, Phys. Lett. B **474**, 15 (2000).
15. R. Rodríguez-Guzmán, J.L. Egido, L.M. Robledo, Phys. Rev. C **62**, 054319 (2000).
16. R. Rodríguez Guzmán, J.L. Egido, L.M. Robledo, Acta Phys. Pol. B **9**, 2385 (2001).
17. R. Rodríguez Guzmán, J.L. Egido, L.M. Robledo, Phys. Rev. C **65**, 024304 (2002).
18. R. Rodríguez Guzmán, J.L. Egido, L.M. Robledo, Phys. Rev. C **62**, 054308 (2000).
19. A. Ozawa, T. Kobayashi, T. Susuki, K. Yoshida, I. Tanihata, Phys. Rev. Lett. **84**, 5493 (2000).
20. J. Decharge, D. Gogny, Phys. Rev. C **21**, 1568 (1980).
21. J.F. Berger, M. Girod, D. Gogny, Nucl. Phys. A **428**, 23c (1984).
22. L.M. Robledo, Phys. Rev. C **50**, 2874 (1994); J.L. Egido, L.M. Robledo, Y. Sun, Nucl. Phys. A **560**, 253 (1993).
23. K. Hara, Y. Sun, Int. J. Mod. Phys. E **4**, 637 (1995).
24. P. Ring, P. Schuck, *The Nuclear Many Body Problem* (Springer, Berlin, 1980).
25. R. Rodríguez-Guzmán, J.L. Egido, L.M. Robledo, Nucl. Phys. A **709**, 201 (2002).
26. J. Dobaczewski, H. Flocard, J. Treiner, Nucl. Phys. A **422**, 103 (1984).
27. J. Dobaczewski, W. Nazarewicz, T.R. Werner, J.F. Berger, C.R. Chinn, J. Dechargé, Phys. Rev. C **53**, 2809 (1996).
28. D. Guillemaud-Mueller, J.C. Jacmart, E. Kashy, A. Latimer, A.C. Mueller, F. Pogueon, A. Richard, Yu.E. Penionzhkevich, A.G. Artuhk, A.V. Belozyorov, S.M. Lukyanov, R. Anne, P. Bricault, C. Détraz, M. Lewitowicz, Y. Zhang, Yu.S. Lyutostansky, M.V. Zverev, D. Bazin, W.D. Schmidt-Ott, Phys. Rev. C **41**, 937 (1990).
29. O. Tarasov, R. Allat, R.C. Angélique, R. Anne, C. Borcea, Z. Dlouhy, C. Donzaud, S. Grévy, D. Guillemaud-Mueller, M. Lewitowicz, S. Lukyanov, A.C. Mueller, F. Nowacki, Yu. Oganessian, N.A. Orr, A.N. Ostrowski, R.D. Page, Yu. Penionzhekevich, F. Pougheon, A. Reed, M.G. Saint-Laurent, W. Schwab, E. Sokol, O. Sorlin, W. Trinder, J.S. Winfield, Phys. Lett. B **409**, 64 (1997).
30. H. Sakurai, N. Aoi, A. Goto, M. Hirai, N. Inabe, M. Ishihara, H. Kobinata, T. Kubo, H. Kumagai, T. Nakagawa, T. Nakamura, M. Notani, Y. Watanabe, Y. Watanabe, A. Yoshida, Phys. Rev. C **54**, R2802 (1996).
31. M. Anguiano, J.L. Egido, L.M. Robledo, Phys. Lett. B **545**, 62 (2002).
32. P.M. Endt, Nucl. Phys. A **633**, 1 (1998).
33. P.M. Endt, Nucl. Phys. A **521**, 1 (1990).
34. P. Raghavan, At. Data Nucl. Data Tables **42**, 189 (1989).
35. E. Caurier, F. Nowacki, A. Poves, J. Retamosa, Phys. Rev. C **58**, 2033 (1998).
36. E. Caurier, F. Nowacki, A. Poves, Nucl. Phys. A **693**, 374 (2001).
37. G. Audi, O. Bersillon, J. Blachot, A.H. Wapstra, Nucl. Phys. A **624**, 1 (1997).
38. F. Sarazin, H. Savajols, W. Mittig, F. Nowacki, N.A. Orr, Z. Ren, P. Roussel-Chomaz, G. Auger, D. Baiborodin, A.V. Belozyorov, C. Borcea, E. Caurier, Z. Dlouhy, A. Gillibert, A.S. Lalleman, M. Lewitowicz, S.M. Lukyanov, F. de Oliveira, Y.E. Penionzhkevich, D. Ridikas, H. Sakurai, O. Tarasov, A. de Vismes, Phys. Rev. Lett. **84**, 5062 (2000).

39. Y. Utsumo, T. Otsuka, T. Mizusaki, M. Honma, Phys. Rev. C **60**, 054315 (1999).
40. T. Otsuka, M. Honma, T. Mizusaki, N. Shimizu, T. Utsumo, Prog. Part. Nucl. Phys. **47**, 319 (2001).
41. A.T. Reed, O. Tarasov, R.D. Page, D. Guillemaud-Mueller, Yu.E. Penionzhkevich, R.G. Allatt, J.C. Angélique, R. Anne, C. Borcea, V. Burjan, W.N. Catford, Z. Dlouhý, C. Donzaud, S. Grévy, M. Lewitowicz, S.M. Lukyanov, F.M. Marqués, G. Martinez, A.C. Mueller, P.J. Nolan, J. Novák, N.A. Orr, F. Pougheon, P.H. Regan, M.G. Saint-Laurent, T. Siiskonen, E. Sokol, O. Sorlin, J. Suhonen, W. Trinder, S.M. Vincent, Phys. Rev. C **60**, 024311 (1999).
42. B.V. Pritychenko, T. Glasmacher, P.D. Cottle, M. Fauerbach, R.W. Ibbotson, K.W. Kemper, V. Maddalena, A. Navin, R. Ronningen, A. Sakharuk, H. Scheid, V.G. Zelevinsky, Phys. Lett. B **461**, 322 (1999).
43. F. Azaiez *et al.*, *Proceedings of the International Conference Nuclear Structure 98*, edited by C. Baktash, AIP Conf. Proc. Vol. **481** (AIP, New York, 1999) p. 243.
44. D. Guillemaud-Mueller, Eur. Phys. J. A **13**, 63 (2002).